Available online at www.sciencedirect.com
ScienceDirect
Journal of Computational Physics 223 (2007) 797–821
JOURNAL OF COMPUTATIONAL PHYSICS
www.elsevier.com/locate/jcp

Reduced dimensional computational models of polymer electrolyte membrane fuel cell stacks

Paul Chang [a], Gwang-Soo Kim [b,1], Keith Promislow [c], Brian Wetton [a,*]

[a] *Mathematics Department, 121-1984 Mathematics Road, UBC, Vancouver, BC, Canada V6T 1Z2*
[b] *Ballard Power Systems, 9000 Glenlyon Parkway Burnaby, BC Canada V5J 5J8*
[c] *Department of Mathematics, MSU East Lansing, MI 48824, USA*

Received 19 January 2006; received in revised form 21 July 2006; accepted 3 October 2006
Available online 27 November 2006

Abstract

A model of steady state operation of polymer electrolyte membrane fuel cell (PEMFC) stacks with straight gas channels is presented. The model is based on a decoupling of transport in the down-channel direction from transport in the cross-channel plane. Further, cross-channel transport is approximated heuristically using one-dimensional processes. The model takes into account the consumption of reactants down the channel, the effect of membrane hydration on its conductivity, water crossover through the membrane, the electrochemistry of the oxygen reduction reaction, thermal transport within the membrane electrode assembly (MEA) and bipolar plates to the coolant, heat due to reaction and condensation and membrane resistance, electrical interaction between unit cells due to in-plane currents in the bipolar plates, and thermal coupling of unit cells through shared bipolar plates. The model corresponds to the typical operation with counter-flowing reactant gas streams. The model is a nonstandard system of non-smooth boundary value differential algebraic equations (DAEs) with strong, nonlocal coupling. A discretization of the system and a successful iterative strategy are described. Some preliminary analysis of the system and iterative strategy is given, using simple, constant coefficient, linear versions of the key components of the model. Representative computational results, validation against existing experimental data and a numerical convergence study are shown.

1. Introduction

Hydrogen is being seriously considered as a major energy carrier for the future [13]. Fuel cells efficiently convert hydrogen to electrical power for automotive and portable applications. Two major benefits of hydrogen fuel cells are their high conversion efficiency and the fact that they have zero emmision (water is the only product of the catalysed reaction of hydrogen and oxygen). A basic introduction to fuel cells can be found in

* Corresponding author. Tel.: +1 604 822 3784; fax: +1 604 822 6074.
E-mail addresses: pchang@pims.math.ca (P. Chang), gwang-soo.kim@intel.com (G.-S. Kim), kpromisl@math.msu.edu (K. Promislow), wetton@math.ubc.ca (B. Wetton).
[1] Present address: Intel Corporation.

0021-9991/$ - see front matter © 2006 Elsevier Inc. All rights reserved.
doi:10.1016/j.jcp.2006.10.011

Nomenclature

a	molar concentration of membrane acid groups, 1200 moles/m^3
A	scaled heat transfer factor to the coolant, value 4000 W/m^2 K
c_a	anode channel water vapour concentration (moles/m^3)
c_c	cathode channel water vapour concentration (moles/m^3)
c_h	anode channel hydrogen concentration (moles/m^3)
c_o	cathode channel oxygen concentration (moles/m^3)
C_{ref}	reference oxygen concentration 40.9 moles/m^3
D_w	membrane free water diffusivity, dependent on water content and temperature (m^2/s)
d_w	fitted constant in expression for D_w (m^2/s), $d_w(T) = 2.1 \times 10^{-7} \exp(-2436/T)$ where T is in Kelvin [4]
D_+	membrane hydronium diffusivity, dependent on water content and temperature (m^2/s)
d_+	fitted constant in expression for D_+ (m^2/s), $d_+(T) = 1.6 \times 10^{-8} \exp(-1683/T)$ where T is in Kelvin [4]
E_0	fitted open circuit voltage 0.944 V
$\mathscr{F}$	Faraday's constant 96,485 C/mole
g	coolant flow rate per unit orthogonal z times its heat capacity, units W/mK, base value 529
H_o	enthalpy of hydronium formation, used in the temperature dependence of K_e, value −52,300 J/mole [33]
H_{vap}	latent heat of vapourization 45,400 J/mole
i	local current density in A/m^2
i_{ref}	fitted oxygen reduction reaction exchange current density 64 A/m^2 [4]
i_T	target average current density for the simulation in A/m^2, an operating condition
$I^{l/l+1}$	current in the bipolar plate between cell l and $l+1$ per unit orthogonal z (A/m)
j	crossover flux of water from anode to cathode (moles/m^2)
k_a, k_c	gas channel scaled pressure drop coefficients, base value 20,000 Pa s/m^3
K_e	ion exchange equilibrium constant in membrane model, depends on temperature, dimensionless
K_o	Base value of K_e, value 6.2
L	cell length 0.67 m
L_m	membrane thickness 50 μ
m, m_+, m_b	membrane free water, hydronium, and bound proton concentrations, scaled by a
m_a, m_c	anode and cathode side values of m
m_a^*, m_c^*	equilibrium values of m_a and m_c
M	number of cells in the stack
n	ratio of nitrogen to oxygen in cathode inlet gas
N	number of discrete points in a uniform discretization of the channel length
p_a, p_c	average anode and cathode channel pressure in Pa
P_{sat}	saturation pressure of vapour, in Pa. Given as an empirical function of temperature in K
s_a, s_c	stoichiometric flow rates of anode and cathode inlet gas streams, dimensionless
$\underline{q} = (q_o, q_c, q_n, q_h, q_a)$	channel molar fluxes (cathode oxygen, cathode water, cathode nitrogen, anode hydrogen and anode water) per unit orthogonal width (z) in moles/m/s
r_a, r_c	anode and cathode channel relative humidities, dimensionless
$\mathscr{R}$	ideal gas constant 8.3143 J/K mole
t	average coolant channel temperature in K
$T_{a,dew}$, $T_{c,dew}$	anode and cathode channel inlet dew points, K
v	local cell voltage
V_{TN}	thermoneutral voltage for ORR 1.28 V
w_a, w_c	anode and cathode channel liquid water fluxes, per unit orthogonal width (z) in moles/m/s
x, y, z	coordinate system down channel, cross-channel, and through MEA (see Fig. 1)

α_c	fitted cathode ORR transfer factor, value 1 (dimensionless)
δ	fitted oxygen mass transport coefficient, 0.8×10^{-3} s mole/mC [4]
γ	fitted vapour mass transport coefficient 0.62×10^{-5} m/s [4]
γ_a, γ_c	condensation rates in the anode and cathode channels, per unit orthogonal z in moles/ms
λ	bipolar plate resistivity $4 \times 10^{-3}\ \Omega$
μ_p, μ_g, μ_m	ratios of thermal conductivity to thickness for the bipolar plates (2300), GDE (5000) and membrane (11,200) in W/m^2 K
ψ	membrane concentration overpotential V
ϕ	membrane potential V
$\underline{\theta} = (\theta_l, \theta_o, \theta_c, \theta_a, \theta_h)$	temperatures in K in the plate adjacent to the coolant (l), in the cathode gas channel (o), at the cathode catalyst sites (c), anode catalyst sites (a) and anode gas channel (h) (see Fig. 2)
θ_m	membrane temperature in K
ω	area-specific membrane resistivity Ω m^2

[20]. A more comprehensive description can be found in [34]. Several important phenomena in polymer electrolyte membrane fuel cells (PEMFC) are reviewed in [36].

Several aspects of PEMFCs are still not well understood at a fundamental level, such as membrane transport, the influence of catalyst layer structure on performance and the nature of two-phase flow (liquid water and gas) in electrodes [36]. However, if one is willing to take parametric descriptions of these phenomena derived from more detailed models and experimental measurements, the question remains how these locally fitted models will combine with more well-understood phenomena of gas and electrical transport to determine overall *system* performance, at the unit cell or stack level.

The earliest PEMFC system models [32,14,27] were for single cells, at steady state under several simplifying assumptions. In [32] only transport through the membrane electrode assembly (MEA) is considered, while in [14,27] transport in gas channels is also considered, coupled locally at each channel location to MEA transport. The reader unfamiliar with fuel cells may wish to consult Figs. 1–3 in Section 2 below. The power of such system level modelling tools for scientific and commercial design was recognized. The major focus for system modelling moved to three-dimensional (3-D) models based on computational fluid dynamics (CFD) codes, see e.g. [6,21–24]. There are certainly valid reasons to turn to 3-D models since there are genuine higher dimensional phenomena in fuel cells, especially gas flow effects connected with serpentine flow fields [21] and two-phase flow effects in the cross plane [24] (these 2-D cross-plane effects were the specific target of the study in [7]). However, at least some of the interest in 3-D codes was the availability of robust CFD software that was seen as a route to solve some of the numerical difficulties associated with developing reduced dimensional models of increasing complexity.

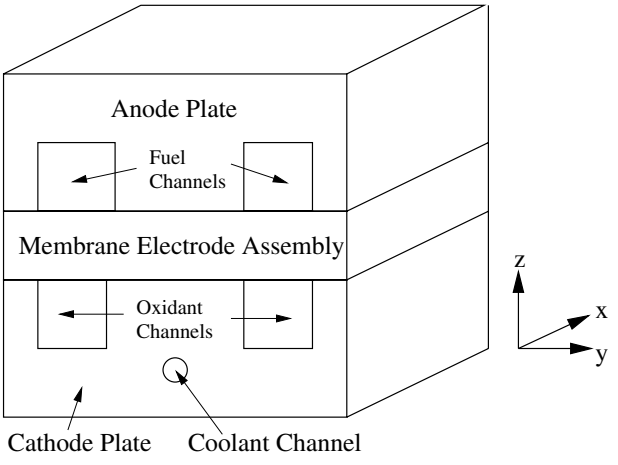

Fig. 1. 3-D schematic of unit fuel cell.

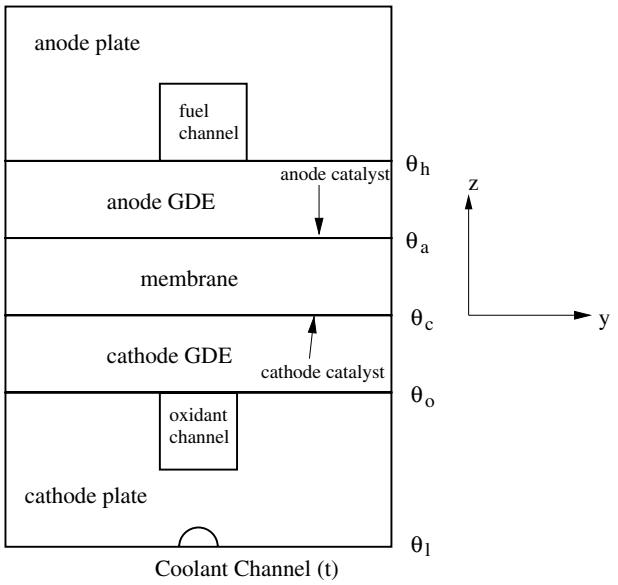

Fig. 2. Cross-section of a unit fuel cell.

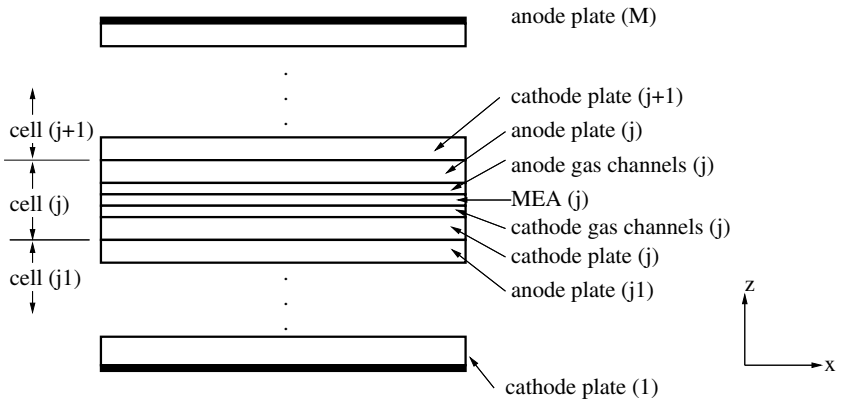

Fig. 3. Cross-section of a fuel cell stack.

In recent years, researchers with more numerical background have returned to the development of more comprehensive reduced dimensional models [11,4,37,39]. These are models that describe a fuel cell with a 1-D model of gas channel flow coupled at each channel location to a 1-D model of through-MEA transport. Our group began with a basic unit cell model of this type [4], using several sets of experimental data for fitting and validation. To this model were added the effects of electrical coupling between unit cells in a stack environment ([3] with validation against experimental results in [18]). Also added were simple models to describe the temperature variations through the MEA and bipolar plates and the increase in coolant temperature in each cell in a fuel cell stack [38,29]. In [12], cell-to-cell variations in solid oxide fuel cells due to thermal affects are considered in a similar way. In the current paper, a reduced dimensional fuel cell stack model is presented with all these effects included. A successful iterative strategy for this complex model is identified. Components of the iterative strategy are analyzed using simple, reduced models. The analysis predicts that the iterative performance is grid independent, which is observed computationally.

This work has two main purposes. First, it describes the successful numerical implementation of a model containing many of the important phenomena of an important new application. Second, it contains a full description of a complex and highly coupled model that can be used as a basis for further analytic and numerical work.

In Section 2, a summary of fuel cell stack geometry and a discussion of the dimensional reductions used in the model is given. In Section 3, the model is presented followed by Section 4 on the discretization and iterative scheme. The analysis of reduced models is given in Section 5. In Section 6, the computational model is validated against a number of historical experimental data sets. In Section 7, sample computations from the model are given that show its power as a design tool. Also, a numerical convergence study is given.

2. Dimensional reduction

Unit fuel cells with straight gas channels (such as the Ballard Mk 9® design) are considered as shown in Fig. 1 (not to scale). Oxidant gas (air) and coolant flow in straight channels in the x direction. The reactant gas (hydrogen) flows in straight channels, either in the $+x$ direction (co-flow operation) or in the $-x$ direction (counter-flow operation). Numerical simulation of counter-flow operation (more common) poses additional computational difficulties as shown below. Unit cells can be of the order of a meter long, but often only a few milli-meters thick.

More detail of the cross-plane ($y-z$) geometry is shown in Fig. 2 (also not to scale). Hydrogen gas moves from channel through the anode gas diffusion electrode (GDE, often a teflonated carbon fibre paper) to the catalyst layer (it is thin enough to be considered as an interface), where Pt particles catalyse its oxidation, producing protons and electrons. The protons cross the membrane (an electronic insulator but protonic conductor such as Nafion®) where they react with oxygen coming from the oxidant channels at the cathode catalyst sites (with the electrons coming through the external circuit) to produce water. This reaction (the oxygen reduction reaction) has a positive potential that provides the electrical power.

The high aspect ratio of a unit cell suggests that the x direction transport is dominated by the gas channel and coolant flow. Furthermore, since the flow is slow enough to be laminar, these flows can be described simply with average quantities in the x direction. This leads to a "2+1 D" model, in which the cross-plane ($y-z$) problem can be solved for each x and connected to 1-D models for the channel flow. It is believed that these models are asymptotically valid. Some preliminary estimates along these lines to justify the 2+1D modelling of thermal transport are given in [29].

In the current work, the cross-plane ($y-z$) problem is further reduced by averaging over y the transport through the membrane and electrodes. A fitted, averaged diffusion parameter (δ) is used to describe diffusive concentration differences of Oxygen from channel averages to catalyst sites. Similarly, a fitted parameter γ describes diffusive effects of water from catalyst sites to channels. Temperature profiles are considered to be constant in y and the values through the unit cell at various locations are denoted by θ with a subscript as shown in Fig. 2.

Unit cells (up to 100 or more) are placed in series to form fuel cell stacks. The anode plate of one cell is placed next to the cathode plate of the next (so that their voltages will add in the stack). The combined plates are called *bipolar* plates. The reduced dimensional geometry of our stack model is shown in Fig. 3.

3. Stack model

Several elements of the model described below have been developed previously: a basic, reduced dimensional unit cell model in [4] with experimental fitting and validation of water crossover and effects of cathode low inlet humidity, simple versions of the thermal model [38,29], the electrical coupling through bipolar plate resistance [3] and its experimental validation [18]. Below, these elements are brought together into a common model with full coupling between them. The numerical handling of the full coupling of the models requires some care.

The equations to be solved are presented in complete detail, although the details of the derivations are left to earlier work where appropriate.

3.1. Fundamental variables

In each unit cell the following quantities are to be determined for each $x \in [0,L]$:

i: local current density in A/m^2.

$\underline{q} = (q_o, q_c, q_n, q_h, q_a)$: channel molar fluxes (cathode oxygen, cathode water, cathode nitrogen, anode hydrogen and anode water) per unit orthogonal width (z) in moles/m/s.
p_a, p_c: average anode and cathode channel pressure in Pa.
t: average coolant channel temperature in K.
$\underline{\theta} = (\theta_l, \theta_o, \theta_c, \theta_a, \theta_h)$: temperatures in K in the plate adjacent to the coolant (l), in the cathode gas channel (o), at the cathode catalyst sites (c), anode catalyst sites (a) and anode gas channel (h).

These variables are found in each unit cell of the stack. The cell index will be denoted by a superscript l.

3.2. Locally determined secondary variables

Several quantities can be determined locally from the fundamental variables using algebraic models.

3.2.1. Gas concentrations in channels

Given the local values of the channel fluxes $\underline{q}$, the channel temperatures θ_o, θ_h, and the channel pressures p_c, p_o it is possible to determine the channel gas concentrations c_o, c_c, c_h and c_a in moles/m^3 using the same subscript notation for fluxes $\underline{q}$ above. It is assumed that the gases are ideal, obey Dalton's law and move in the channel with a common velocity. Consider first the cathode gas channel. There are two cases to consider, depending on whether the cathode channel gases are saturated or unsaturated.

Assume first that the cathode channel is unsaturated and compute

$$c_o = \frac{p_c}{\mathscr{R}\theta_o}\frac{q_o}{q_o + q_c + q_n}, \tag{1}$$

$$c_c = \frac{p_c}{\mathscr{R}\theta_o}\frac{q_c}{q_o + q_c + q_n}. \tag{2}$$

where $\mathscr{R}$ is the ideal gas constant. Note that the first term on the right of both equations above represents the total molar concentration of gas at the cathode channel temperature and pressure and the second term represents the fraction of this concentration the gas type occupies based on its fraction of the total flux. More detailed description of this flux to concentration map can be found in [4].

If the value of c_c computed above is greater than $P_{sat}(\theta_o)/(\mathscr{R}\theta_o)$ (where P_{sat} is the saturation pressure of vapour as a function of temperature for which an empirical fit is available [32]) then the cathode channel gases are over-saturated. In this case, it is assumed that vapour will condense to prevent over-saturation and the concentrations c_o and c_c above are replaced with the following values:

$$c_o = \frac{p_c - P_{sat}(\theta_o)}{\mathscr{R}\theta_o}\frac{q_o}{q_o + q_n}, \tag{3}$$

$$c_c = \frac{P_{sat}(\theta_o)}{\mathscr{R}\theta_o}. \tag{4}$$

The cathode liquid water flux w_c can also be determined

$$w_c = q_c - \frac{c_c}{c_o}q_o \tag{5}$$

which would be zero in the dry case discussed in the preceding paragraph. The cathode channel relative humidity is given by

$$r_c = \frac{c_c\mathscr{R}\theta_o}{P_{sat}(\theta_o)}. \tag{6}$$

Similarly, anode quantities c_h, c_a, w_a and r_a can be computed.

3.2.2. Membrane transport

It is assumed that the membrane is made of Nafion® or similar material. The material parameters described below are specifically fitted to Nafion®. Water crossover through the membrane from anode to cathode j,

membrane area-specific resistivity ω, and the so-called concentration overpotential ψ can be determined from a detailed one-dimensional transport and chemical model based on ideas in [33] that can be solved analytically [4]. The analytic solution can only be found for the case of a locally (in x) isothermal membrane and so for convenience the average temperature

$$\theta_m = (\theta_a + \theta_c)/2$$

is used.

In the model, the membrane contains uncharged, "free" water molecules (concentration m) and water that carries an extra proton (hydronium concentration m_+). The concentrations are normalized to the molar concentration of acid groups in the membrane material, denoted by a. Consider distance through the membrane normalized to $z \in [0,1]$ with $z = 0$ the cathode catalyst layer. In the model used here, protons are carried as hydronium, which corresponds to an electro-osmotic drag factor of unity. The higher electro-osmotic drag factors seen in liquid water equilibrated membranes [35] are not included in our approach.

In the model, it is assumed that the membrane water transport is dominated by diffusion

$$\frac{d}{dz}\left(D_w(m,\theta_m)\frac{dm}{dz}\right) = 0, \tag{7}$$

where as indicated the diffusivity D_w depends on both water content and temperature. The diffusivity is taken to be linearly proportional to free water content [5]:

$$D_w = d_w(\theta_m)m. \tag{8}$$

In this case, the free water profile can be written as

$$m(z) = \sqrt{m_c^2 + (m_a^2 - m_c^2)(z-1)}, \tag{9}$$

where m_a and m_c are the anode and cathode side boundary values for the free water content determined below. The profile gives the crossover flux:

$$j = \frac{i}{\mathscr{F}} + a d_w(T)\frac{(m_a)^2 - (m_c)^2}{2L_m}. \tag{10}$$

The first term represents the water transported as hydronium to carry the current. The second term is the diffusive flux, where the scaling terms a and the membrane thickness L_m have been added to give a dimensional quantity.

At equilibrium, the membrane free water content is determined by the relative humidity r of the surrounding gas. The correlation for Nafion® in [32]:

$$m^* = 0.043 + 17.81r - 39.85r^2 + 36r^3 \tag{11}$$

is used. This expression can be used to determine both anode m_a^* and cathode m_c^* side equilibrium contents from the anode r_a and cathode r_c channel relative humidities. It should be noted that the relationship above holds for vapour equilibrated membranes. When the membrane is in contact with liquid water, the membrane water content jumps to a higher level (the so-called Schroeder's paradox [35]). This phenomena is not included in the present model.

If equilibrium values are used as Dirichlet conditions for (7), unrealistically dry membrane conditions at cathode inlet are predicted by the model. A simple mass transfer mechanism of vapour movement from catalyst sites to channels with fitted parameter γ [4] is assumed:

$$\frac{j}{a} = \gamma(m_a^* - m_a) \tag{12}$$

$$\frac{j}{a} + \frac{i}{2\mathscr{F}} = \gamma(m_c - m_c^*). \tag{13}$$

On the left hand side of (13) above, the additional term represents the water produced by the reaction, which must also leave the ionomer material of the catalyst layer. For given r_a and r_c, values of m_a^* and m_c^* are

computed. Given also i and θ_m, Eqs. (10), (12) and (13) can be solved for m_a and m_c, leading to a value for j and the free water profile $m(z)$ in (9). Algebraic manipulation leads to

$$m_c = \frac{1}{2}(\xi_+ + \xi_-), \tag{14}$$

$$m_a = \frac{1}{2}(\xi_+ - \xi_-), \tag{15}$$

where

$$\xi_+ = m_c^* + m_a^* + \frac{i}{2\gamma a \mathscr{F}},$$

$$\xi_- = \frac{m_c^* - m_a^* + \frac{5i}{2\gamma a \mathscr{F}}}{1 + \frac{d_w(T)\xi_+}{L_m \gamma}}.$$

If the resulting cathode water content m_c from (14) is greater than the maximum allowed at equilibrium (m^* from (11) with $r = 1$) then an alternate solution is used. The cathode content is taken to be the maximum and the anode content is solved to match the flux condition (12). An algebraic formula is available for this case also. Recent work [25] shows that mechanical constraint of the membrane serves to cap its water content at levels below the liquid isotherms even when it is in contact with liquid water, consistent with the approach taken above. Note that a slight error is made in the formulae above, assuming that the free water content is the total water content $m + m_+$ for equilibrium values and as used in the expression for D_w. Note further that a single value γ is used for both absorption and desorption of water from the membrane in this model. Recent work [15] suggests different terms should be used for the two phenomena. Our value of γ can be considered to be fit for the dominant cathode desorption rate.

Following again the ideas of [33] presented in [4] the hydronium concentration m_+ and bound (to the SO_3^- acid groups of Nafion) proton m_b concentrations are balanced by an ion exchange equilibrium:

$$SO_3^- H^+ + H_2O \rightleftharpoons SO_3^- + H_3O^+.$$

The equilibrium can be written mathematically as

$$m_b m K_e(\theta_m) = m_+(1 - m_b), \tag{16}$$

where the equilibrium constant has the form

$$K_e(\theta_m) = K_0 \exp\left[-\frac{H_0}{\mathscr{R}}\left(\frac{1}{\theta_m} - \frac{1}{298}\right)\right].$$

The assumption of electroneutrality leads to

$$1 - m_+ - m_b = 0. \tag{17}$$

Combining (17) with (16) leads to

$$m_+ = -\frac{K_e m}{2} + \sqrt{\left(\frac{K_e m}{2}\right)^2 + K_e m}. \tag{18}$$

Using the profile (9) in (18) gives the hydronium concentration $m_+(z)$ through the membrane. A balance for charge transport by hydronium in the membrane is given by the Nernst–Plank equation:

$$-\frac{D_+}{L_m}\frac{dm_+}{dz} - \frac{\mathscr{F}}{\mathscr{R}\theta_m} D_+ m_+ \frac{d\phi}{dz} = \frac{i}{a}, \tag{19}$$

where the a and L_m terms appear due to the previous scaling of m_+ and z. We take the hydronium diffusivity D_+ to be dependent on θ_m and linearly dependent on water content m with a similar form as (8) above. In (19) all terms are known but $\phi(z)$. Integrating over z the following is obtained:

$$\phi(1) - \phi(0) = \omega i - \psi, \tag{20}$$

where ω is the membrane area-specific resistivity

$$\omega = \frac{\mathscr{R}\theta_m L_m}{a\mathscr{F}^2 d_+(\theta_m)} \int_0^1 \frac{dz}{m(z)m_+(z)} \tag{21}$$

and ψ is a concentration overpotential:

$$\psi = \frac{\mathscr{R}\theta_m}{\mathscr{F}} \ln\left(\frac{m_+(1)}{m_+(0)}\right). \tag{22}$$

Although the relationships above have many details, they can be considered conceptually as algebraic maps from inputs of local values of θ_a, θ_c, r_a, r_c and i to outputs of local values of j, ω and ψ. That the maps are algebraic, except for one numerical quadrature for (21), allows for fast computations since this map must be computed at every iteration for every grid point in every cell in the stack. However, more complicated 1-D MEA models that can only be solved numerically on a grid can also be used in the unit cell and stack framework.

3.2.3. Voltage

The local cell voltage is given as

$$v = E_0 - i\omega + \psi - \frac{\mathscr{R}\theta_c}{\mathscr{F}\alpha_c} \ln\frac{iC_{ref}}{i_0(c_o - \delta i)}, \tag{23}$$

where E_0 is the open circuit voltage (taken from measurements) at reference oxygen concentration C_{ref}, and the second and third terms on the right describes the voltage drop in the membrane derived in (20) above. The final term is the overpotential that describes losses due to the irreversibility of the reaction [26]. At very low current densities, there are additional terms that modify the logarithm to give the open circuit E_0 in the limit. The parameters α_c (transfer factor), δ (mass transfer parameter) and i_{ref} (reference current) are fitted parameters.

In the last term on the right hand side $c_o - \delta i$ approximates the oxygen concentration at catalyst sites, lower than the channel average because the oxygen must diffuse through the GDL and catalyst layer to the active sites. The concentration reduction should be proportional to the flux, which is proportional to the local current, leading to the given form. Note that this form implies there is a maximum local current that can be drawn, equal to c_o/δ. The mass transfer parameter can be considered to be due to diffusion through a media with effective length L_{eff}:

$$\delta = \frac{L_{eff}}{D_{eff} 4\mathscr{F}},$$

where the factor $4\mathscr{F}$ is the conversion from current density to oxygen molar flux. In reality, there are several diffusive effects in series lumped in to this parameter.

3.3. Differential algebraic equations

3.3.1. Thermal transport

In the simple model derived below, the thicknesses of the gas and coolant channels are neglected and the heating due to channel condensation and overpotential losses are taken to be concentrated at interfaces. Under these assumptions and the underlying assumption of one-dimensionality (y) of through-MEA transport, the local thermal profiles through the plate and MEA are piecewise linear (quadratic through the membrane when uniform ohmic heating is assumed). The following thermal balances result:

$$\mu_p(\theta_o - \theta_l) + \mu_g(\theta_o - \theta_c) = H_{vap}\gamma_c \tag{24}$$

$$\mu_g(\theta_c - \theta_o) + \mu_m(\theta_c - \theta_a) = (V_{TN} - v - \omega i/2)i \tag{25}$$

$$\mu_g(\theta_a - \theta_h) + \mu_m(\theta_a - \theta_c) = \frac{1}{2}\omega i^2 \tag{26}$$

$$\mu_p(\theta_h - \theta_l) + \mu_g(\theta_h - \theta_a) = H_{vap}\gamma_a \tag{27}$$

$$\mu_p(\theta_o^l - \theta_l^l) + \mu_p(\theta_h^{l-1} - \theta_l^l) = A(\theta_l^l - T^l) \tag{28}$$

at cathode channel, cathode catalyst, anode catalyst, anode channel and coolant channel, respectively. Specifically, the RHS of (24) and (27) are the heating due to channel condensation. Some algebra shows that the uniform ohmic heating in the membrane results is equivalent to an equal distribution of the heat to the anode and cathode sides as shown in the RHS of (25) and (26). On the cathode side (25) are also the irreversible losses of the electrochemical reaction $(V_{TN} - v - \omega i)i$. Here, V_{TN} is the thermo-neutral voltage of the oxygen reduction reaction with product vapour, μ_p, μ_g and μ_m are the ratios of thermal conductivity to thickness for the plates, electrodes and membrane, respectively. The parameter A is a scaled Nusselt number from conjugate heat transfer theory (see [29] for details). The physical parameter H_{vap} is the heat of vapourization and γ_a, γ_c are the condensation rates of the anode and cathode channel streams. These are given by:

$$\gamma_a = -\frac{dw_a}{dx}, \tag{29}$$

$$\gamma_c = \frac{dw_c}{dx}. \tag{30}$$

In the last Eq. (28), heat fluxes into the coolant come from different cells and so the cell number superscripts are used explicitly. From Fig. 3 it is clear that the coolant of cell l receives heat from the cathode side of cell l and the anode side of cell $l-1$.

3.3.2. Electrical coupling

Differences in local current densities lead to in-plane currents in the bipolar plates. The in-plane currents in the bipolar plate between cells l and $l+1$ are labelled $I^{l/l+1}$ as shown in Fig. 4. These current are the integrals (in z) of the x-directional current density. From current conservation the following is obtained:

$$\frac{dI^{l/l+1}}{dx} = i^l(x) - i^{l-1}(x). \tag{31}$$

In-plane resistance of the bipolar plate λ (per unit length to currents per unit width) leads to changes in the cell voltage:

$$\frac{dv^l}{dx} = \lambda(-I^{l/l+1} + I^{l-1/l}). \tag{32}$$

Relationships (31) and (32) should be clear from Fig. 4. Differentiating (32) and using (31) the plate currents can be eliminated, leading to the so-called *fundamental voltage equation*:

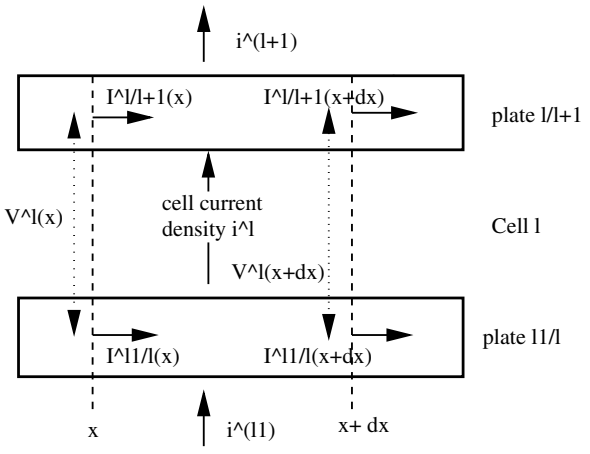

Fig. 4. Diagram showing the derivation of Eqs. (31) and (32).

$$\frac{\mathrm{d}^2 v^l}{\mathrm{d}x^2} - \lambda(i^{l-1} - 2i^l + i^{l+1}) = 0. \tag{33}$$

A similar relationship is derived in [19].

3.4. Channel conservation and transport

In each cell, the following channel flux equations represent the effects of gas consumption and water production and cross-over:

$$\frac{\mathrm{d}q_\mathrm{o}}{\mathrm{d}x} = -\frac{i}{4\mathscr{F}} \tag{34}$$

$$\frac{\mathrm{d}q_\mathrm{h}}{\mathrm{d}x} = +\frac{i}{2\mathscr{F}} \tag{35}$$

$$\frac{\mathrm{d}q_\mathrm{c}}{\mathrm{d}x} = +\frac{i}{2\mathscr{F}} + j \tag{36}$$

$$\frac{\mathrm{d}q_\mathrm{a}}{\mathrm{d}x} = j \tag{37}$$

The cathode nitrogen flux is constant. Note that the case of counter-flowing gas streams is considered: cathode gas flow is from left to right but anode is from right to left. However, anode fluxes are considered to be positive, hence the sign change in (35), (37).

Assuming laminar flow in the channels and viscosities independent of pressure, temperature and composition (reasonable, see [28]) it is appropriate to take the local pressure drop proportional to volumetric flow rate:

$$\frac{\mathrm{d}p_\mathrm{c}}{\mathrm{d}x} = -k_\mathrm{c}(q_\mathrm{o} + q_\mathrm{c} + q_\mathrm{n} - w_\mathrm{c})\frac{\mathscr{R}\theta_\mathrm{o}}{p_\mathrm{c}} \tag{38}$$

$$\frac{\mathrm{d}p_\mathrm{a}}{\mathrm{d}x} = +k_\mathrm{a}(q_\mathrm{h} + q_\mathrm{a} + -w_\mathrm{a})\frac{\mathscr{R}\theta_\mathrm{h}}{p_\mathrm{a}} \tag{39}$$

where k_a and k_c are experimentally measured channel gas flow resistance parameters with units s/m^3. As above, the sign change in the second term is due to the anode counter-flow. Note that the liquid water flux does not contribute to the pressure gradient in this model. Standard two-phase channel flow models (see e.g. [10]) are not appropriate for the small, capillary dominated flows found in hydrophobic fuel cell channels. Experimental work is under way to identify appropriate handling of the effect of channel liquid water on pressure drop, including extreme phenomena such as channel flooding.

Coolant flow is taken to be from left to right (same direction as the cathode channel gas flow). Taking into account the heat flowing in to the coolant,

$$g\frac{\mathrm{d}t^l}{\mathrm{d}x} = \mu_\mathrm{p}(\theta_\mathrm{o}^l + \theta_\mathrm{h}^{l-1} - 2\theta_\mathrm{l}^l), \tag{40}$$

where g is the product of coolant heat capacity and flow rate (per unit orthogonal direction z). Notice that in this equation the cell number superscripts appear.

3.5. Boundary, end cell and global conditions

3.5.1. Boundary conditions

The only boundary conditions independent of operating conditions are the following:

$$\frac{\mathrm{d}v}{\mathrm{d}x}(0) = 0, \tag{41}$$

$$\frac{\mathrm{d}v}{\mathrm{d}x}(L) = 0 \tag{42}$$

for each cell. These represent the fact that cell ends are electrically insulated.

3.5.2. Operating conditions

Since the unit cells of the stack are connected in series, the same total current runs through each of them. The total current is specified as an equivalent target average current density i_T. A global condition for the model is that

$$\frac{1}{L}\int_0^L i^l(x)\,\mathrm{d}x = i_T \tag{43}$$

for each cell l.

Inlet reactant fluxes are specified as stoichiometric ratios s_a and s_c of the minimum molar flux to produce this current:

$$q_o(0) = s_c \frac{i_T}{4\mathscr{F}} L, \tag{44}$$

$$q_h(L) = s_a \frac{i_T}{2\mathscr{F}} L. \tag{45}$$

The constant cathode nitrogen flux is determined by the ratio of nitrogen to oxygen in the inlet stream:

$$q_n = n q_o(0)$$

where $n \approx 0.79/0.21$ for dry air at standard conditions which has approximately 21% oxygen and 79% nitrogen (and very small amounts of other trace elements). The scaled coolant flow rate g, its inlet temperature $T(0)$, and the inlet pressures $p_c(0)$ and $p_a(L)$ must also be given.

The cathode inlet water flux is dependent on the humidification of the inlet stream, often expressed as a dew point temperature (a vapour partial pressure equivalent to saturated conditions at this temperature). If $T_{c,dew}$ is the given cathode inlet dew point, then

$$q_c(0) = (n+1) q_o(0) \frac{P_{sat}(T_{c,dew})}{p_c(0) - P_{sat}(T_{c,dew})}.$$

The water flux at anode inlet $q_a(L)$ can be determined similarly from its inlet dew point $T_{a,dew}$.

Note that s_a, s_c, and g can be given different values in different cells in the stack.

A somewhat subtle point is that additional information must be specified at inlet if the channel conditions are saturated (which is determined by the model). Typical operating conditions have unsaturated inlet gases, so this issue does not arise in the computations shown in this work. An allowable additional condition when the inlet gas stream is saturated is that there is no condensation at inlet, which has the benefit of matching the condition for dry inlet gases. However, the exact processes at inlet that act over an asymptotically small region have been lost in the dimensional reduction of the model.

3.6. End cell conditions

M cells form the stack, numbered $l = 1, \ldots, M$. Again, using the Ballard Mk 9 design as a template, an additional coolant channel $l = M + 1$ is added to the anode side of cell M.

In this paper, the end plates are taken to be infinitely electrically conductive and thermally insulated. The modifications to handle end plates of finite resistance are discussed in [3]. More realistic thermal end plate conditions are the subject of current research by the authors.

The electrical end plate boundary conditions can be expressed in terms of ghost values for i^0 and i^{N+1} in (33):

$$i^0 = i^1 \tag{46}$$

$$i^{M+1} = i^M. \tag{47}$$

Note that these conditions used in (33) integrated over x and using boundary conditions (41) and (42) show that the total current through each cell is the same. Thus (43) is a single global constraint as expected.

The thermal end plate boundary conditions can be expressed in terms of ghost values for θ_h^0 and θ_o^{M+1} in (28) and (40):

$$\theta_{\mathrm{h}}^{0} = \theta_{\mathrm{l}}^{1}, \tag{48}$$

$$\theta_{\mathrm{o}}^{M+1} = \theta_{\mathrm{l}}^{M+1}. \tag{49}$$

3.7. System description and important coupling

There are two main difficulties to the fuel cell stack system presented above, besides just the complexity of detail of physical phenomena it represents:

Nonlocality. There are two types of nonlocality in the model. The first arises from the voltage/current coupling (33). Note that this equation looks like a partially discretized elliptic operator and so it is appropriate to describe this as *elliptic* coupling. The second type is due to the counterflow operation: even if the elliptic components of the model were specified, it cannot be considered as an initial value DAE, but rather as a boundary value DAE. The DAE is of index 1, so except for the point raised below, can be considered to add no real additional difficulty to the computation [1].

Lack of smoothness. The lack of smoothness in the model arises from the change between saturated and unsaturated conditions in the flux to concentration map described in Section 3.2.1. This lack of smoothness also corresponds to a change in the DAE structure of the problem. When the channel is saturated, derivative terms appear in (24) and (27) and channel temperatures change from algebraic to differential variables. A second source of non-smoothness is the transition in the membrane solve from value (14) to the pinned maximum value. This is not handled explicitly in the current code.

The three important couplings in the model are listed below:

1. The non-local coupling of current density to cathode oxygen concentration through flux consumption (34) to concentration (1) or (3) to the concentration dependence of voltage (23) and its nonlocal influence back to current densities (33). This coupling is especially strong when the local current density is near its maximum value (i near c_{o}/δ in (33)).
2. The nonlocal coupling of channel relative humidity to the water crossover (10) through the relationships of Section 3.2.2 leads to changes in water fluxes (36) and (37) and so back to channel relative humidities through (2) or (4) and then (6). The nonlocality arises from the counterflow operation of the gas streams.
3. The local coupling of channel condensation to channel temperature when the channel (anode or cathode) is saturated. Channel temperatures strongly affect channel water fluxes (5) through (4). Channel condensation is the derivative of water flux (30) and is a large heating source in the determination of channel temperatures (24).

Simplified models (linear, constant coefficient) of these coupling mechanisms above and the analysis of their behaviour in our iterative approach are given in Section 5 below. The last mechanism above motivated our choice of semi-implicit discretization described in Section 4.1 below, in which the channel temperature and liquid water flux are handled with an implicit solve.

The overall strategy is to break the model into computationally and analytically manageable pieces. The local current densities are taken as the primary variables. For given values of the local current densities, channel fluxes and thermal profiles can be considered as a boundary value DAE with the elliptic coupling removed. From the solution of this problem, cell voltages can be computed and residuals in (33) determined. In this way, the fuel cell model can be described as a non-local equation of nonstandard character for the current densities. Note that it is also possible to consider the problem with the cell voltages as the primary variables. It was necessary to use this formulation to match the experimental conditions in [18].

The existence and uniqueness of solutions to the model is an open question. The model can certainly fail to have solutions if a target current i_{T} is specified greater than the limit allowed by electrode oxygen mass transport. At extremely low inlet humidification conditions, fuel cells have been shown to have multiple steady state solutions [2]. The computational results shown in Section 7 are based on conditions away from these extreme cases.

4. Numerical approximation

4.1. Discretization

The channel is discretized on a regular grid on $[0, L]$ with $N + 1$ points with spacing $\Delta x = L/N$. Algebraic conditions (1)–(6), (10)–(15), (20)–(28) apply at each grid point. First order forward difference approximation is used for the derivatives in anode condensation (29), cathode gas fluxes (34) and (36), and cathode pressure (38). First order backward difference approximation is used for the derivatives in cathode condensation (30), anode gas fluxes (35) and (37), anode pressure (39), and coolant temperature (40). The second order derivatives in (33) are approximated with centered differences and the ghost points introduced are eliminated using the boundary conditions (41) and (42). The resulting discrete approximation of the system (33) is consistent but rank deficient of order one. One equation of the system is replaced by a trapezoidal rule approximation to (43) in one cell. The expression (23) is regularized at currents near and past the maximum current as described in [3].

The use of first order one-sided differencing approximation and the lack of smoothness in the flux to concentration map at saturation points (it is Lipchitz continuous but not differentiable) limits the accuracy of the approximation to $O(\Delta x)$. Given the state of accuracy of the underlying models and the engineering application, this is acceptable.

4.2. Iterative solution strategy

As foreshadowed in Section 3.7, the iterative strategy is based on an outer iteration on discrete local current densities. For given current densities, the DAE boundary value problems for the channel fluxes, channel pressure and coolant temperatures are solved by back and forth shooting [9]. Details of the iterative strategy are given below. It should be noted that several variants on the iterative strategy have been implemented, and the following is the most robust. Some analytic insight into the iterative approach is given in Section 5.

4.2.1. DAE boundary value problem

In the back and forth shooting strategy, the anode and cathode channel fluxes and pressures are updated in an alternating fashion. When the cathode channel fluxes are updated, the anode channel fluxes, pressure and concentrations are held fixed. Similar cathode quantities are held fixed during the anode update. The coolant channel temperature is updated during the cathode update, and is held fixed during the anode update. The temperatures $\underline{\theta}$ are updated in both directions.

In the cathode update, cathode fluxes and pressures are updated with explicit approximation of (34), (36), and (38) in each cell. With the channel fluxes and pressures (and the local current held fixed from the outer iteration) given at the next grid point, a nonlinear problem for $\underline{\theta}$ and t in all cells remains. Given an initial guess for these quantities and assuming for now that the cathode conditions will be unsaturated, (1), (2) and (6) can be used to compute cathode concentrations and relative humidities. Membrane quantities can be determined from the algebraic relationships in Section 3.2.2 and the cell voltage can also be computed from (23) for each cell. In this way, residuals in (24)–(28) and the implicit discretization of (40) can be computed and $\underline{\theta}$ and t for each cell adjusted to satisfy the system of equations. If at convergence the unsaturated cathode assumption is not satisfied for particular cells, the solve is conducted assuming these cathodes are saturated. The iteration scheme is an approximate Newton approach, ignoring the weak dependence of resistivity ω and cell voltage v (that enter the RHS of Eqs. (25) and (26)) on the temperatures in the computation of the Jacobian. However, when channels are saturated, the dependence of water flux on channel temperature and hence its influence on condensation rate γ_c computed by difference formulae that enter (24) must be used in the approximate Jacobian to obtain convergent iterations. At cathode inlet, a reduced system is solved, using the fixed inlet coolant temperature t. The cathode sweep is followed by an equivalent anode sweep using fixed coolant temperatures and cathode conditions.

4.2.2. Current density update

For given discrete current densities, the DAE problem can be iteratively solved as above. The solution of this problem provides the voltage v at all points and all the quantities in (23). Residuals in the discrete

equation (33) can be computed. An approximate Newton step that preserves the stack current is used to update the discrete current densities. The approximate Jacobian used for the update uses a local approximation of voltage sensitivities to current density, that is $\partial v_j^l/\partial i_{j'}^{l'}$ (where the subscript is the discrete channel location) is taken nonzero only when $l = l'$ and $j = j'$ and its value is just the explicit derivative of v from (23) with i evaluated at the given values of ω, c_o, $i=_j^l$ and θ_c.

4.2.3. Initialization

Initialization was done with uniform current density i_T and channel fluxes equal to inlet values. A preliminary, reduced channel solve was performed with all temperatures held constant, equal to the inlet coolant temperature. This was followed by full channel and current density iterations described above. In the runs conducted with the computational model for the parameters given, it was found that this initialization was sufficient to obtain overall convergence. In potentially more computationally challenging parameter regimes, a continuation approach could be used.

4.3. Co-flow model

The model and computational method for the case of counter-flowing channel gases was presented above since it is much more complicated than the co-flow reactant gas case. When anode and cathode gases are configured to run in the same direction, the channel component of the method described above becomes a standard, initial value DAE that can be solved from inlet to outlet without iteration.

4.4. Implementation

Early versions of the computational model were implemented in MATLAB. In order to make the computational tool faster and more portable and retain graphical interfaces, a version in java was implemented.

5. Simplified analysis

There are three key elements to the iterative procedure: the local approximation of voltage sensitivity in the current updates, the use of back and forth shooting for water crossover, and the use of back and forth shooting to compute temperature profiles that include the effects of channel condensation heating. The first two of these elements are examined in turn below using constant coefficient continuum models. The analysis shows the channel discretization independence of the iterative schemes and the limits of applicability of the schemes in terms of parameter ranges.

5.1. Local approximation of voltage sensitivity

A reduced, constant coefficient linear model is constructed below that preserves the structure of the nonlocal coupling of local current densities to channel oxygen concentrations. The iterative scheme of updating local current densities using local voltage sensitivities is examined using this model.

A stack is considered with some idealizations: it is taken to be isothermal at temperature θ, the channels are taken to be everywhere saturated, the membrane resistivity ω is taken to be constant and the concentration overpotential ψ in (23) is neglected. With these simplifications, the anode channel can be removed from the model since it no longer impacts performance. In each cell, there is oxygen consumption (34), the relation at saturation of oxygen concentration to flux (3), and the local voltage relationship (23). The fundamental voltage equation (33) connects cells.

Assume that all cells operate at the same cathode stoich s_c. The quantities i, c_o, q_o and v are relabelled to represent the *difference* to a base solution. These are vector quantities with entries for each cell but the superscript l for cell number has been suppressed. The relationship (34) is linearized at inlet channel conditions and (23) is linearized at inlet channel conditions and average current density i_T. Further, x is scaled so that the channel length L is unity. The following system results:

$$\frac{\mathrm{d}q_\mathrm{o}}{\mathrm{d}x} = -C_1 i \tag{50}$$

$$c_\mathrm{o} = C_2 q_\mathrm{o} \tag{51}$$

$$v = -C_3 i + C_4 c_\mathrm{o} \tag{52}$$

$$\frac{\mathrm{d}^2 v}{\mathrm{d}x^2} - \lambda L^2 \mathbf{A} i = 0 \tag{53}$$

where C_1, C_2, C_3 and C_4 are positive constants given below:

$$C_1 = \frac{L}{4\mathscr{F}}$$

$$C_2 = \frac{p_\mathrm{c} - P_\mathrm{sat}(\theta)}{\mathscr{R}\theta} \frac{n}{(n+1)^2} \frac{1}{q_\mathrm{o}(0)}$$

$$C_3 = \omega - \frac{\mathscr{R}\theta}{\alpha_\mathrm{c}\mathscr{F}} \left(\frac{1}{i_\mathrm{T}} + \frac{\delta}{c_* - \delta i_\mathrm{T}} \right)$$

$$C_4 = \frac{\mathscr{R}\theta}{\alpha_\mathrm{c}\mathscr{F}} \frac{1}{c_* - \delta i_\mathrm{T}}.$$

Above, c_* is the oxygen concentration at inlet

$$c_* = \frac{p_\mathrm{c} - P_\mathrm{sat}(\theta)}{\mathscr{R}\theta} \frac{1}{1+n}.$$

The matrix $\mathbf{A}$ acts locally (in x) on the M vector of local currents for the M cells: $(\mathbf{A}i)^l = i^{l-1} - 2i^l + i^{l+1}$ for $l \neq 1, M$ and $(\mathbf{A}i)^1 = i^2 - i^1$, $(\mathbf{A}i)^M = i^{M-1} - i^M$ using the end conditions described in Section 3.6. Boundary conditions $v'(0) = v'(1) = 0$ apply in each cell and initial conditions $q_\mathrm{o}(0) = 0$. Since i represents differences to base currents,

$$\int_0^1 i(x)\,\mathrm{d}x = 0 \tag{54}$$

in each cell.

The iterative scheme for the local current densities can be described in this linear framework as

$$\frac{\mathrm{d}q_\mathrm{o}^{(n+1)}}{\mathrm{d}x} = -C_1 i^{(n)} \tag{55}$$

(the update of fluxes based on previous current densities) in each cell where the bracketed superscript denotes iteration level. These fluxes, using relationship (51), and the as yet unknown local current densities determine the voltage at the next iteration:

$$v^{(n+1)} = -C_3 i^{(n+1)} + C_2 C_4 q_\mathrm{o}^{(n+1)}. \tag{56}$$

The new current densities are chosen such that $v^{(n+1)}$ above satisfies Eq. (53) and the boundary conditions for the voltage. This system can be written:

$$-C_3 i^{(n+1)''} - C_5 i^{(n)'} - \lambda L^2 \mathbf{A} i^{(n+1)} = 0, \tag{57}$$

where $C_5 = C_1 C_2 C_4$. To proceed, note that $\mathbf{A}$ is symmetric with eigenvalues α_l for $l = 0, \cdots N-1$ that lie in the interval $(-4, 0]$ ($\mathbf{A}$ is the second-order finite difference derivative operator with first-order approximation of Neumann boundary conditions). Solutions to (57) are sought of the form

$$i^{(n)}(x) = i(x)\mathbf{e}_l G^n,$$

where G is a scalar, $i(x)$ is a scalar function and $\mathbf{e}_l$ is the lth eigenvector of $\mathbf{A}$. Eq. (57) becomes

$$Gi'' + C_6 i' + C_7 G \alpha_l i = 0, \tag{58}$$

where $C_6 = C_5/C_3$ and $C_7 = \lambda L^2/C_3$. This boundary value problem has the boundary conditions $G\,i' + C_6 i = 0$ at $x = 0,1$ (inherited from $v' = 0$) and can be considered as a generalized eigenvalue problem for G, the iterative scheme growth factor. For $\alpha_l = 0$ the boundary conditions are dependent and the system is augmented with the integral condition (54).

Using standard techniques for boundary value problems, G is found to be always imaginary with values

$$G = \frac{\hat{\imath} C_6}{2} \frac{1}{\sqrt{n^2\pi^2 - C_7\alpha_l}}, \tag{59}$$

for n nonzero integers. The term $\hat{\imath}$ is used for $\sqrt{-1}$ to distinguish it from the current. The eigenfunctions are a shifted Fourier cosine series. Note that the largest value of $|G|$ occurs for $n = 1$ and $\alpha_l = 0$. Thus, the outer electrical iterations will converge when the dimensionless number

$$\Omega = \frac{C_6}{2\pi}$$

is less than one. This number represents the ratio of local to global influence of current density on voltage.

The value of Ω is estimated as follows. A fixed membrane area-specific resistivity $\omega = 1 \times 10^{-5}\ \Omega\ \mathrm{m}^2$ is used (recall that in the reduced model of this section, the dependence of membrane resistivity on hydration is not considered). Standard Ballard Mk9® conditions are considered: temperature $\theta = 350$ K, cathode pressure $p_c = 3 \times 10^5$ Pa, target current density $i_T = 10{,}000\ \mathrm{A/m^2}$ and cathode inlet stoichiometric flow rate $s_c = 2$. The following is obtained

$$\Omega \approx 0.088.$$

This explains the almost Newton-like convergence of the outer iterations.

Note that the form of (59) predicts that neither higher wavenumber modes (from finer discretizations) nor the number of cells M in the stack limit the convergence rate of this aspect of the iterative solution strategy. This matches computational evidence of convergence independent of grid refinement. The signature of the $\Omega > 1$ instability in computations would be iterative growth of a low-wavenumber mode ($M = 1$) uniform in all cells of the stack ($\alpha_l = 0$).

5.2. Water crossover

In this section, one element of the "back and forth" shooting strategy is considered: the convergence in anode and cathode channel water flux due to crossover. The analysis that follows corresponds to regions of the cell where both anode and cathode channels are dry. Since crossover is limited to one cell, it is sufficient to consider a single cell in the stack to analyze the performance of the iterations. During these iterations, the local current density is given and held fixed. A linear, constant coefficient model is constructed as above by linearizing the channel water flux to relative humidity map (2) and (6) at inlet conditions and given current density i_T. The cell is again considered to be at uniform temperature θ. The anode and cathode relative humidities determine the diffusive flux. This relationship is also linearized and the quantities below represent *differences* to the base solution:

$$j = C_1 r_a - C_2 r_c \tag{60}$$

$$r_a = C_3 q_a \tag{61}$$

$$r_c = C_4 q_c \tag{62}$$

$$\frac{dq_a}{dx} = Lj = C_5 q_a - C_6 q_c \tag{63}$$

$$\frac{dq_c}{dx} = Lj = C_5 q_a - C_6 q_c \tag{64}$$

where C_1–C_6 are positive constants described below and the channel has been scaled to unit length as above. The constants C_1 and C_2 (with units moles/m^2/s) could theoretically be determined analytically through the formulae in Section 3.2.2 but it is more practical to determine them by numerical differentiation at given

current i_T, temperature θ and common anode and cathode base relative humidity r. From formulae (2) and (6) and similar formulae for the anode,

$$C_3 = \frac{p_a(1)}{P_{sat}(\theta)} \frac{q_h(1)}{(q_h(1)+q_a(1))^2},$$
$$C_4 = \frac{p_c(0)}{P_{sat}(\theta)} \frac{q_o(0)+q_n(0)}{(q_o(0)+q_n(0)+q_c(0))^2},$$

where $q_c(0)$ and $q_a(1)$ are determined to match the given base relative humidity r. The remaining dimensionless constants

$$C_5 = LC_1C_3$$
$$C_6 = LC_2C_4$$

represent the strength of coupling of anode and cathode water fluxes through membrane crossover.

The iterative strategy applied to (63) and (64) is the following:

$$\frac{dq_c^{(n+1)}}{dx} = C_5 q_a^{(n)} - C_6 q_c^{(n+1)} \tag{65}$$
$$\frac{dq_a^{(n+1)}}{dx} = C_5 q_a^{(n+1)} - C_6 q_c^{(n+1)} \tag{66}$$

with $q_c^{(n)}(0) = 0$ and $q_a^{(n)}(1) = 0$ (recall, at this level, these fluxes are considered to be differences to a base solution). This corresponds to anode conditions held fixed while the cathode fluxes are updated from right to left. This is followed by an anode flux update from left to right.

The system (65) and (66) can be reduced (after an iteration index shift) to a higher order system in q_c alone:

$$q_c^{(n+1)''} + (C_6 - C_5) q_c^{(n+1)'} + C_5C_6(q_c^{(n)} - q_c^{(n+1)}) = 0. \tag{67}$$

Allowing a slight abuse of notation, the form

$$q_c^{(n)}(x) = G^n q(x)$$

is assumed, leading to

$$q'' + (C_6 - C_5)q' + C_5C_6\left(\frac{1}{G} - 1\right)q = 0 \tag{68}$$

with $q(0) = 0$ and $q'(1) + C_6 q(1) = 0$. This again is a boundary value problem that can be solved with standard methods to give

$$G = \frac{C_5C_6}{C_5C_6 + \frac{1}{4}(C_6 - C_5)^2 + \mu^2}, \tag{69}$$

where μ takes the nonzero discrete values that solve

$$\mu \cos\mu + \frac{1}{2}(C_6 + C_5)\sin\mu = 0. \tag{70}$$

The eigenfunctions q are a nonstandard, exponentially weighted sine series.

It is clear from (69) that G is real and positive with $G < 1$. Thus, this iteration scheme always converges. The largest value of G is obtained from the smallest root μ of (70). As in the result above, the higher wavenumber modes converge more quickly. Thus, the performance of the discrete iterative scheme is predicted (and observed) to be grid independent. An estimate of the maximum value of G, assuming $\theta = 350$, $r = 0.81$ for anode and cathode (corresponding to $T_{dew} \approx 345$ K), anode and cathode pressures of 3×10^5 Pa, and inlet conditions for anode and cathode stoichiometric flow rates of $s_a = s_c = 2$, leads to

$$G_{max} \approx 0.073.$$

An alternate iterative strategy for channel fluxes in counterflow operation was proposed in [37]. It can be analyzed similarly to the steps above and the prediction is that the method is unstable. The authors of [37] report that under-relaxation of their scheme is required (but that performance is still reasonable in this case).

6. Validation

A large, historical experimental data set based on Ballard Power Systems Mk 9® hardware is available. This data was used to fit and validate preliminary versions of the model [4,18]. Some of these validation studies are summarized briefly below, demonstrating that the complete stack model developed here can capture many phenomena of interest. In the following section, more speculative computations are given, showing the power of the model as a simulation tool for understanding fuel cell operation and virtual design optimization.

6.1. Unit cell

In Fig. 5, comparisons between model and experimental results of global quantities are shown. These include polarization curves (graphs of cell voltage versus average current density) for both air and pure oxygen operation and also total water crossover (the net amount of water leaving the anode as a fraction of the water produced by the current). In Fig. 6, comparison between model and experimental results of local current density and its dependence on cathode stoichiometric flow rate and humidification are shown. Details of the experimental conditions for this data are given in [4].

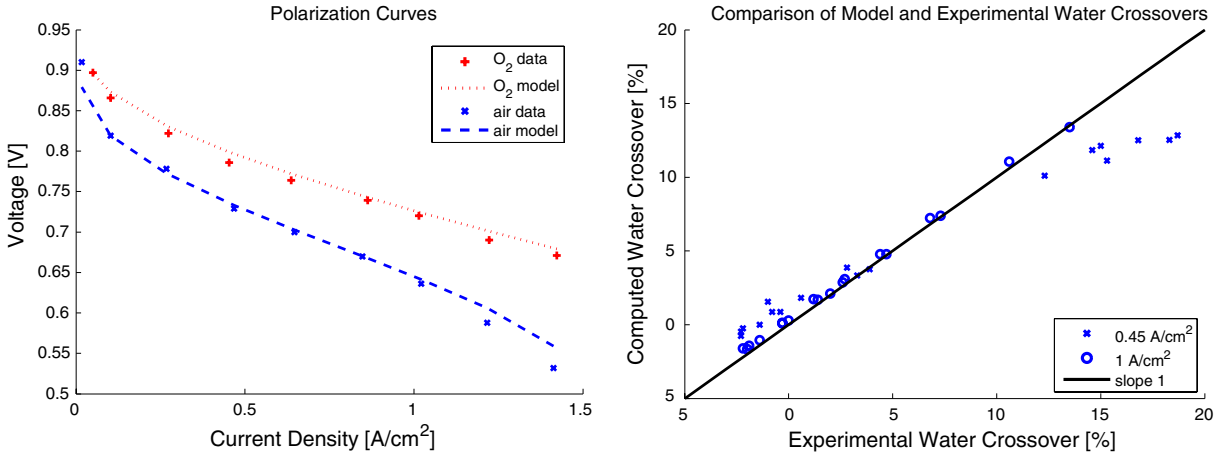

Fig. 5. Validation of unit cell polarization curves and total water crossover.

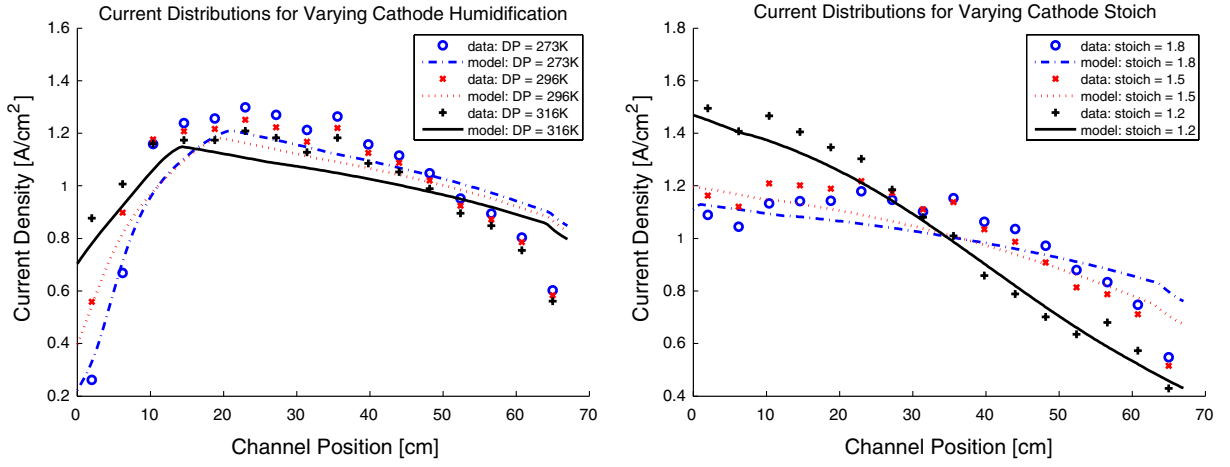

Fig. 6. Validation of unit cell current density profiles and their dependence on cathode inlet stoichiometric flow rate and humidification.

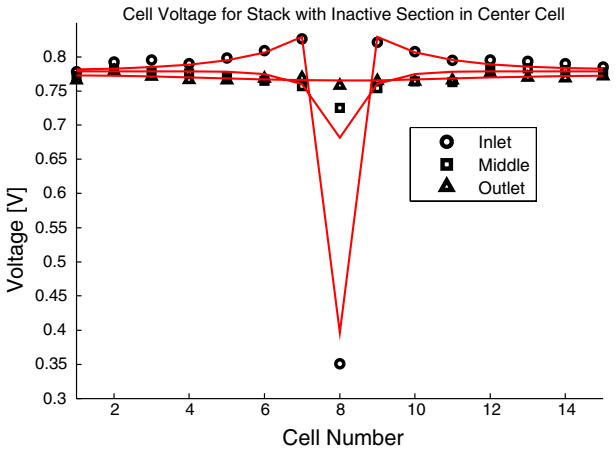

Fig. 7. Validation of voltage variations in a stack with an anomalous centre cell.

6.2. Electrical coupling

In Fig. 7 a comparison between the model and experimental results on the effects of electrical coupling between cells in a stack is given. A short stack of 15 cells is used for the experiment. The centre cell (#8) has an anomaly created by covering the third of the active area of the cell near the cathode inlet with a non-conducting layer. Current from the neighbouring cells in this region is forced around this region and the resulting currents in the bipolar plates create the voltage variations shown in the figure. Details of the experimental conditions for this data are given in [18].

6.3. Future validation

Experimental work is in progress to validate the thermal coupling aspect of the model. Still missing are validation studies that incorporate several of the phenomena coupled together. All the experimental data available is purposely targeted to validate a single aspect of the model. Consider the extreme anomalies in Section 7.2. It is shown that the large electrical anomaly considered there does not lead to significant thermal anomalies. Also, the large thermal anomaly case does not lead to significant changes in current density. A different situation in which a large thermal anomaly does not lead to significant changes in local current density in the stack setting is shown experimentally in recent work [31].

If one includes the effects of liquid water, there are several possible strong interactions between thermal and electrical effects. Consider for example the situation at end cells: they are cooler due to convective heat loss from their surfaces. Thus, end cells tend to have more liquid water in their gas channels. This liquid water impedes reactant gas flow from gas headers, leading to lower stoichiometric flow and anomalous current density profiles. We believe we can include these effects and capture this kind of phenomena in future versions of the model in the framework developed here.

7. Computational results

7.1. Unit cell results

We consider a base case with the following operating conditions:

- $p_a = 3.2 \times 10^5$ Pa
- $p_c = 3 \times 10^5$ Pa
- $s_a = 1.2$

- $s_c = 1.8$
- $t(0)$=343 K
- $i_T = 10{,}000$ A/m^2 (1 A/cm^2).
- $g = 529$ W/m K.
- $T_{a,dew} = 336$ K
- $T_{c,dew} = 336$ K
- counterflow operation.

Four changes to these base conditions are considered:

reduced cathode flow: $s_c = 1.2$
reduced coolant flux: g halved
co-flow operation
reduced inlet humidity (dry) cathode: $T_{c,dew} = 296$ K

In Fig. 8 the cathode channel temperature and the local current density is shown for the base case, cathode understoich, and reduced coolant runs. Fig. 9 shows the same plots for the base case, co-flow, and dry cathode

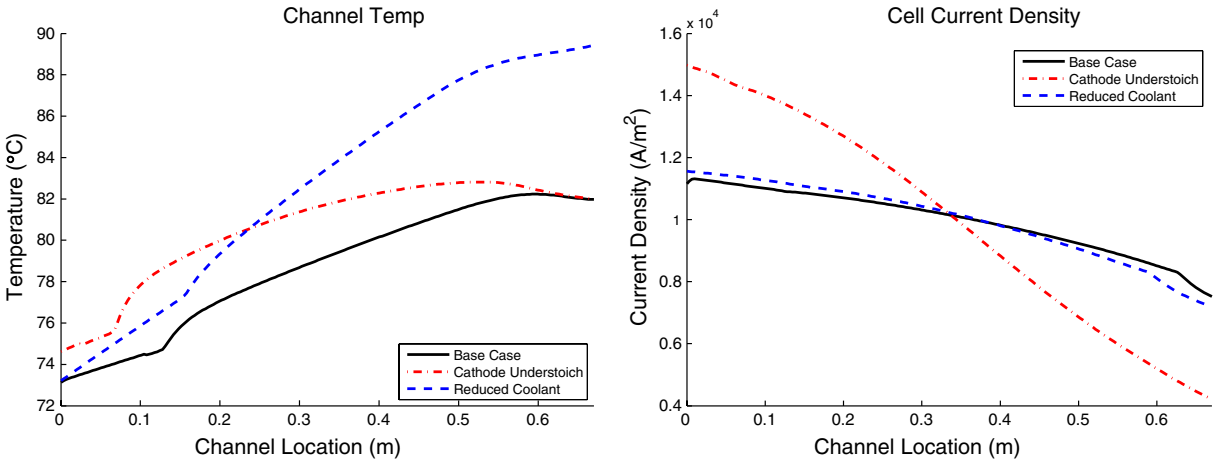

Fig. 8. Unit cell computational results showing the base case, cathode understoich, and reduced coolant runs.

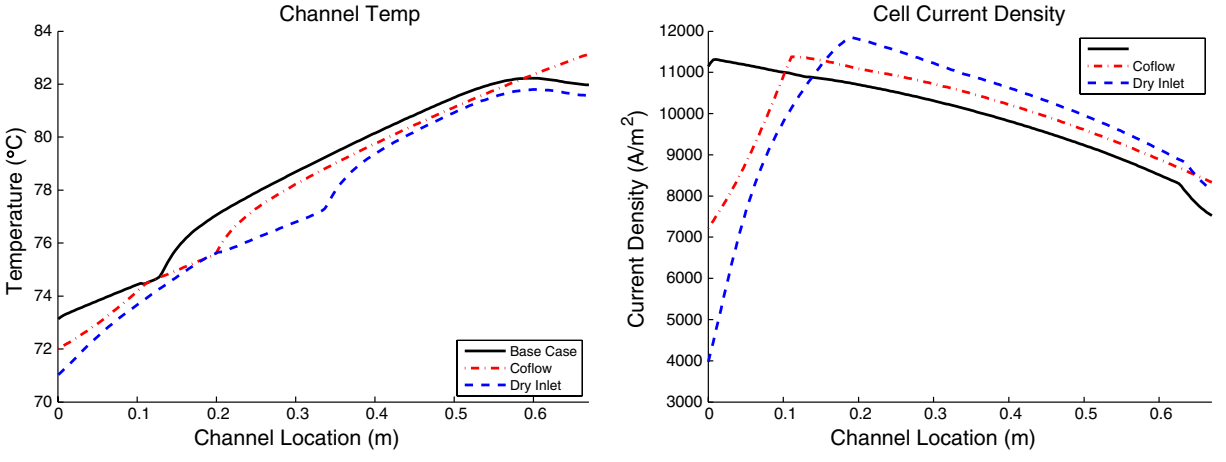

Fig. 9. Unit cell computational results showing the base case, co-flow, and dry cathode inlet runs.

inlet runs. In Fig. 8 higher temperatures are seen for the reduced coolant case as expected but also for the reduced cathode inlet flow rate: less oxygen means the cell operates less efficiently and generates more heat. The reduced oxygen flow rate case also features a current density profile skewed towards inlet, where the channel oxygen concentration remains high. In the reduced coolant case, the higher temperatures make the cathode dryer at outlet (more water crosses over to hydrate the inlet hydrogen stream). The dryer membrane at outlet has higher resistance and the current density shifts towards inlet.

In Fig. 9 most of the structure is due to humidification effects. The dry cathode inlet causes a higher membrane resistivity (lowering local current) in a region near inlet before the cathode gas saturates. In the co-flow case, the combination of under-saturated anode and cathode leads to a similar but smaller effect. Note that in all three cases the abrupt change in channel temperature slope occurs where the cathode channel saturates and condensation heating begins. In the counterflow runs, the dip in temperature at outlet corresponds to the evaporative cooling of water leaving the saturated cathode channel and crossing over to the dryer anode inlet.

7.2. Stack results

A stack of $M = 13$ cells (with 14 bipolar plates and coolant channels) is considered with a discretization of $N = 100$ points down the channel. All cells but the centre #6 are run at base conditions. The centre cell is run at anomalous conditions. The results of the centre cell run at reduced cathode flow rate $s_c = 1.2$ are shown in

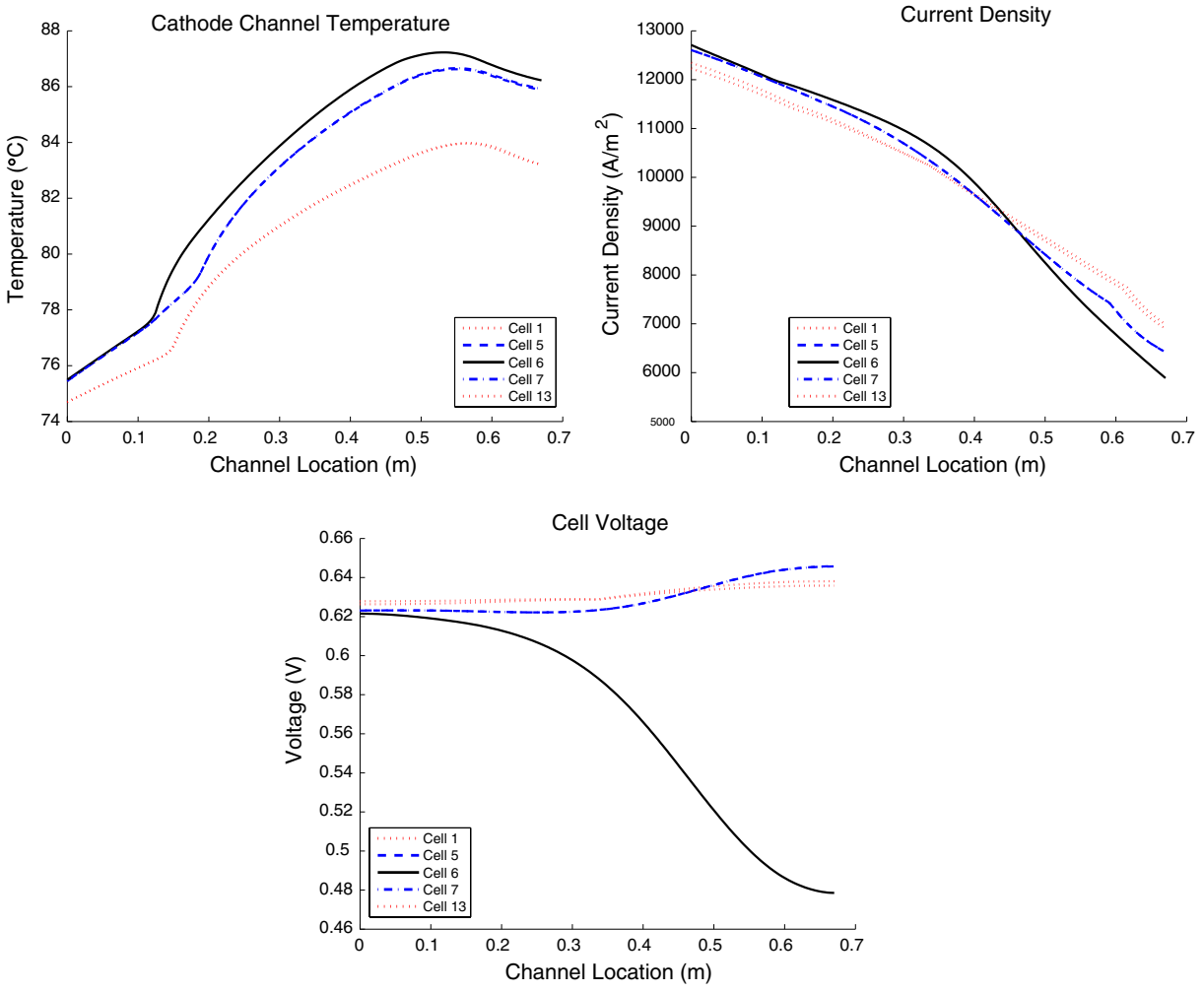

Fig. 10. Stack computational results of an anomalous centre cell with reduced cathode inlet gas flow rate.

Table 1
Maximum norm differences of discrete solutions on grids with N and $2N$ points

N	i	θ_o
200	17.2285	0.044222
400	8.6456	0.022609

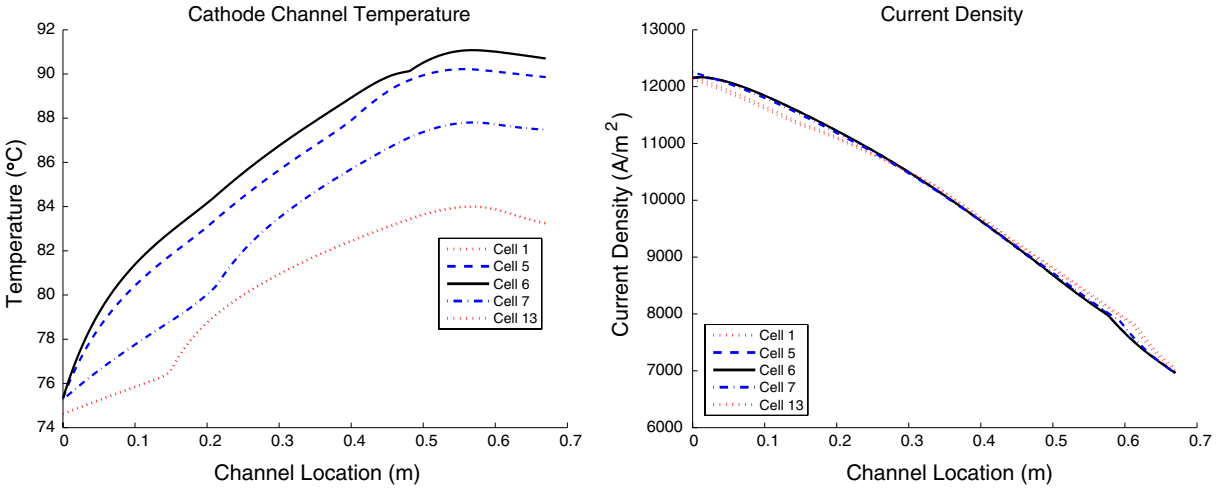

Fig. 11. Stack computational results of an anomalous centre cell with reduced coolant flow rate.

Fig. 10. Because of the electrical coupling through shared bipolar plates, the local current density of the anomalous cell is not the same as that of the equivalent low stoich isolated unit cell shown in Fig. 8. Its effect extends over adjacent cells as predicted by the simple theory presented in [3]. Note that the voltage also has significant variation.

Using the anomalous cathode flow rate case above, a numerical convergence study is performed. Approximate errors are obtained by comparing the solutions on grids of N and $2N$ points. Maximum norm errors are shown in Table 1 for cathode channel temperature θ_o and current density i. First order convergence is clearly seen.

In Fig. 11 a second stack run is shown using an anomalous centre cell with reduced (by half) coolant flow rate. Because of the thermal coupling through shared bipolar plates, the effect on the temperature of the anomalous cell is decreased from that of the equivalent low coolant flow rate isolated unit cell shown in Fig. 8. Although the end plates are thermally insulated, the temperatures at the end cells are cooler than the interior cells due to the extra coolant channel at the ends.

8. Summary and future work

A comprehensive model of a PEMFC stack has been presented. The model contains many aspects important to fuel cell operation. A robust implementation is given. The main contribution of this work is the separation of the complex model into computationally manageable pieces. The computational method is backed by some simplified analysis and a convergence study.

Several elements of this stack model have been experimentally validated. Good agreement with unit cell experimental data for polarization curves, overall water crossover and also current density under variations of air flow rate and humidification is obtained. Good agreement is also obtained for electrical coupling of an anomalous centre cell in a small stack. Experimental work on stack level thermal coupling that could validate this aspect of the model is in progress.

The most important missing aspects to the model are liquid water transport in channels and electrodes, thermal end cell effects and flow sharing effects between cells from shared gas headers. Prototype versions

of the stack computational model add in more realistic thermal end plate effects. Flow sharing effects through inlet headers has also been considered [8], similar to the approach taken in [17]. The development of a stack model that features a more realistic description of transport in the electrodes including liquid water and its slow transients following the analytic work in [30] is currently under way. The effect of channel liquid water on pressure drop (that will change the reactant flow to each cell through header coupling) is not readily amenable to theoretical study. To be able to include these effects, empirical fits to experimental data would be needed.

References

[1] U. Ascher, L. Petzold, Computer Methods for Ordinary Differential Equations and Differential–Algebraic Equations, SIAM, 1988.
[2] J. Benziger, E.J. Chia, I.G. Kevrekidis, Water balance and multiplicity in a polymer electrolyte membrane fuel cell, AIChE J. 50 (2004) 2320–2324.
[3] P. Berg, A. Caglar, J. St.-Pierre, K. Promislow, B. Wetton, Electrical coupling in proton exchange membrane fuel cell stacks: mathematical and computational modelling, IMA J. Appl. Math. 71 (2006) 241–261.
[4] P. Berg, K. Promislow, J. St.-Pierre, J. Stumper, B. Wetton, Water management in PEM fuel cells, J. Electrochem. Soc. 151 (2004) A341–A353.
[5] D.M. Bernardi, M.W. Verbrugge, A mathematical model of the solid-polymer electrolyte fuel cell, J. Electrochem. Soc. 139 (1992) 2477–2491.
[6] T. Berning, N. Djilali, A 3D, multiphase, multicomponent model of the cathode and anode of a PEM fuel cell, J. Electrochem. Soc. 150 (2003) A1598–A1607.
[7] E. Birgersson, M. Noponen, M. Vynnycky, Analysis of a two-phase non-isothermal model for a PEFC, J. Electrochem. Soc. 152 (2005) A1021–A1034.
[8] P. Chang, J. St.-Pierre, J. Stumper, B. Wetton, Flow distribution in proton exchange membrane fuel cell stacks, J. Power Sources 162 (2006) 340–355.
[9] T. Eirola, Convergence of the back-and-forth shooting method, J. Optim. Theor. Appl. 41 (1983) 559–572.
[10] A.C. Fowler, Models in the Applied Sciences, Cambridge University Press, 1997.
[11] S.A. Freunberger, M. Santis, I.N. Schneider, A. Wokaun, F.N. Buechi, In-plane effects in large-scale PEMFCs: model formulation and validation, J. Electrochem. Soc. 153 (2006) A396–A405.
[12] A.C. Burt, I.B. Celik, R.S. Gemmen, A.V. Smirnov, A numerical study of cell-to-cell variations in a SOFC stack, J. Power Sources 126 (2004) 76–87.
[13] National Hydrogen Energy Roadmap, Department of Energy Report, November, 2002. <http://www.hydrogen.energy.gov/>.
[14] T.F. Fuller, J. Newman, Water and thermal management in solid-polymer-electrolyte fuel cells", J. Electrochem. Soc 140 (1993) 1218–1225.
[15] S. Ge, X. Li, B. Yi, I.M. Hsing, Absorption, desorption, and transport of of water in polymer electrolyte membranes for fuel cells, J. Electrochem. Soc. 152 (2005) A1149–A1157.
[17] G. Karimi, J.J. Baschuk, X. Li, Performance analysis and optimization of PEM fuel cell stacks using flow network approach, J. Power Sources 147 (2005) 162–177.
[18] G.-S. Kim, J. St.-Pierre, K. Promislow, B. Wetton, Electrical coupling in PEMFC stacks, J. Power Sources 152 (2005) 210–217.
[19] A.A. Kulikovsky, Voltage loss in bipolar plates in a fuel cell stack, J. Power Sources 160 (2006) 431–435.
[20] J. Larminie, A. Dicks, Fuel Cell Systems Explained, Wiley, 2003.
[21] W-k. Lee, S. Shimpalee, J.W. Van Zee, Verifying predictions of water and current distributions in a serpentine flow-field PEMFC, J. Electrochem. Soc. 150 (2003) A341–A348.
[22] S. Mazumder, J.V. Cole, Rigorous 3-D mathematical modelling of PEM fuel cells: I. Model predictions without liquid water transport, J. Electrochem. Soc. 150 (2003) A1503–A1509.
[23] S. Mazumder, J.V. Cole, Rigorous 3-D mathematical modelling of PEM fuel cells: II. Model predictions with liquid water transport, J. Electrochem. Soc. 150 (2003) A1510–A1517.
[24] D. Natarajan, T. Nguyen, Three-dimensional effects of liquid water flooding in the cathode of a PEM fuel cell, J. Power Sources 115 (2003) 66–80.
[25] I. Nazarov, K. Promislow, The impact of membrane constraint on PEM fuel cell water management, J. Electrochem. Soc. (submitted).
[26] J. Newman, K.E. Thomas-Alyea, Electrochemical Systems, third ed., Wiley, Hoboken, 2004.
[27] T.N. Nguyen, R.E. White, A water and heat management model for proton exchange membrane fuel cells, J. Electrochem. Soc. 140 (1993) 2178–2186.
[28] B.C. Poling, J.M. Prausnitz, J.P. O'Connell, The Properties of Gases and Liquids, fith ed., McGraw-Hill, New York, 2001.
[29] K. Promislow, B. Wetton, A. Simple, Mathematical model of thermal coupling in fuel cell stacks, J. Power Sources 150 (2005) 129–135.
[30] K. Promislow, J. Stockie, B. Wetton, A sharp interface reduction for multiphase transport in a porous fuel cell electrode, Proc. Roy. Soc. A 462 (2006) 789–816.

[31] M. Santis, S.A. Freunberger, M. Papra, A. Wokaun, F.N. Buechi, Experimental Investigation of Coupling Phenomena in Polymer Electrolyte Fuel Cell Stacks (preprint).
[32] T.E. Springer, T.A. Zawodzinski, S. Gottesfeld, Polymer electrolyte fuel cell model, J. Electrochem. Soc. 138 (1991) 2334–2341.
[33] T. Thampan, S. Malhotra, H. Tang, R. Datta, Modelling of conductive transport for PEMs for fuel cells, J. Electrochem. Soc. 147 (2000) 3242–3250.
[34] W. Vielstich, A. Lamm, H.A. Gasteiger (Eds.), Handbook of Fuel Cells: Fundamentals, Technology and Applications, VCH-Wiley, Weinhein, 2003.
[35] A.Z. Weber, J. Newman, Transport in polymer-electrolyte membranes, I: physical model, J. Electrochem. Soc. 150 (2003) A1008–A1015.
[36] A.Z. Weber, J. Newman, Modeling transport in polymer-electrolyte fuel cells, Chem. Rev. 104 (2004) 4679–4726.
[37] A.Z. Weber, R.M. Darling, J. Newman, Modeling two-phase behaviour in PEFCs, J. Electrochem. Soc. 151 (2004) A1715–A1727.
[38] B. Wetton, K. Promislow, A. Caglar, A simple thermal model of PEM fuel cell stacks, in: Proceedings of the Second International Conference on Fuel Cell Science, Engineering and Technology, Rochester, June, 2004.
[39] J.S. Yi, T.V. Nguyen, An along-the-channel model for proton exchange membrane fuel cells, J. Electrochem. Soc. 145 (1998) 1149–1159.